

# The Structural Basis of T4 Phage Lysis Control: DNA as the Signal for Lysis Inhibition

Inna V. Krieger<sup>1</sup>, Vladimir Kuznetsov<sup>1,†</sup>, Jeng-Yih Chang<sup>1,2</sup>, Junjie Zhang<sup>1,2</sup>, Samir H. Moussa<sup>1,2,‡</sup>, Ryland F. Young<sup>1,2</sup> and James C. Sacchettini<sup>1</sup>

<sup>1</sup> - Department of Biochemistry and Biophysics, Texas A&M University, College Station, TX 77843, USA

<sup>2</sup> - Center for Phage Technology, Department of Biochemistry and Biophysics

**Correspondence to James C. Sacchettini:** at: Department of Biochemistry and Biophysics, Texas A&M University, 301 Old Main Dr, College Station, TX 77843, USA. [sacchett@tamu.edu](mailto:sacchett@tamu.edu)

<https://doi.org/10.1016/j.jmb.2020.06.013>

Edited by Owen Pornillos

## Abstract

Optimal phage propagation depends on the regulation of the lysis of the infected host cell. In T4 phage infection, lysis occurs when the holin protein (T) forms lesions in the host membrane. However, the lethal function of T can be blocked by an antiholin (RI) during lysis inhibition (LIN). LIN sets if the infected cell undergoes superinfection, then the lysis is delayed until host/phage ratio becomes more favorable for the release of progeny. It has been thought that a signal derived from the superinfection is required to activate RI. Here we report structures that suggest a radically different model in which RI binds to T irrespective of superinfection, causing it to accumulate in a membrane as heterotetrameric 2RI–2T complex. Moreover, we show the complex binds non-specifically to DNA, suggesting that the gDNA from the superinfecting phage serves as the LIN signal and that stabilization of the complex by DNA binding is what defines LIN. Finally, we show that soluble domain of free RI crystallizes in a domain-swapped homotetramer, which likely works as a sink for RI molecules released from the RI–T complex to ensure efficient lysis. These results constitute the first structural basis and a new model not only for the historic LIN phenomenon but also for the temporal regulation of phage lysis in general.

© 2020 The Author(s). Published by Elsevier Ltd. This is an open access article under the CC BY-NC-ND license (<http://creativecommons.org/licenses/by-nc-nd/4.0/>).

## Introduction

There is significant interest in the use of phage-based therapeutics as treatments for multiple-drug-resistant bacterial infections [1], and thus, knowledge on how phage infections are controlled is important. In double-stranded DNA phages, the length and fecundity of the infection cycle are determined by small membrane proteins called holins and their specific regulators, the antiholins [2]. Holins initiate lysis by permeabilizing the cytoplasmic membrane at a genetically programmed time, setting in motion a lysis pathway that results in release of the viral progeny. [3]. It has been shown that the T4 phage holin is produced from the late genes and accumulates harmlessly in the membrane until the optimal time for lysis [3]. While holins are composed primarily

of transmembrane  $\alpha$ -helices [4], the holin from the T4 phage (T) is somewhat unique among the identified holins as having substantial cytoplasmic (~32 residues) and periplasmic (~150 residues) domains with only a single transmembrane domain [3]. It is the polymerization of these transmembrane domains that leads to the formation of lesions in the membrane, which allows phage peptidoglycan-degrading enzymes into the periplasmic space leading to the cell lysis. While the steps of lysis are clear, the precise molecular mechanism is not well understood.

To avoid premature lysis and optimize the outcome of an infection, the polymerization of the holin is tightly regulated. The periplasmic and cytoplasmic antiholins, RI and RIII, regulate T4 holin function by binding to its soluble domains [5–8]. RI has a signal arrest and release (SAR) domain at its N terminus, so that it is

secreted to the periplasm in a membrane-tethered form and then released from the bilayer [9]. The SAR domain has been shown to quantitatively exit the bilayer when the membrane potential collapses [10].

Lysis inhibition (LIN) is a phenomenon first discovered in the 1940s by the Delbrück phage group [11] and linked to superinfection [12]. A superinfection refers to a viral attack on an already infected cell. It has been suggested that a superinfection induces LIN because there are fewer hosts than phage in the media, a time when it is not advantageous to release the new progeny. While the mechanism that triggers LIN is not known, LIN occurs even when the infected bacteria contains assembled viral particles and amounts of holin and endolysin sufficient for lysis [3]. The superinfection is aborted when the 170 kb DNA and the internal capsid proteins of superinfecting phage are blocked from entering the cytoplasm by periplasmic proteins deployed by the primary phage [13]. The DNA of the superinfecting phage is trapped in the periplasm where it is degraded by nucleases [13]. It has been proposed that a signal from the superinfecting phage is detected, leading to lysis inhibition through the stabilization of the RI antiholin protein from the primary phage [5]. RI is unstable once released from the membrane; its exposed SAR domain is recognized by periplasmic protease DegP resulting in rapid degradation of RI [9]. In this scenario, stabilization of RI in response to a superinfection leads to an increase in the content of free periplasmic RI, which would bind to the periplasmic domain of T and prevent it from making holes. However, there is very little known about the molecular basis of a superinfection, stabilization of RI, and interplay between RI and the holin T resulting in LIN.

Following on our previous work on characterizing T4 lytic proteins [6], we now report the crystal structures of the periplasmic/soluble domain of the antiholin RI (sRI) and of the complex between sRI and the periplasmic domain of the holin T (sT) to contribute to a molecular understanding of the mechanism of lysis and LIN in T4. This structural information has led to the identity of the signal for LIN. The results are discussed in terms of a new model for the T4 lysis pathway and for the mechanism of LIN.

## Results

### The structure of the RI antiholin periplasmic domain in free form

The periplasmic domain of the RI antiholin (residues 25 to 92, sRI) with a C-terminal His-tag was recombinantly expressed in Shuffle® *Escherichia coli* cells, which have been shown to facilitate disulfide bond formation and increase protein solubility. The protein was purified to greater than 95% homogeneity and crystallized. Crystals formed in the hexagonal  $P6_{22}$  space group with one molecule of sRI in the asymmetric unit. The crystal structure of sRI was solved by the single anomalous dispersion (SAD) method using selenomethionine-modified protein (Table 1). The structure was refined to 2.2 Å resolution, and the final model had an  $R_{work} = 28.4\%$  and  $R_{free} = 32.3\%$  with good stereo chemistry.

The sRI refined structure consists of three  $\alpha$ -helices (Figure 1(a)). The first two helices (H1: residues 27–44 and H2: residues 46–66) look like a single long  $\alpha$ -

**Table 1.** Crystallographic data and refinement statistics

Data collection				
	sRI	sRI-sT (Se-Met)	sRI-sT	sRI-sT $\Delta\alpha 0$
PDB ID	6PSH	6PSK	6PXE	6PX4
Space group	$P6_{22}$	$P6_{522}$	$P2_1$	$R3_2:H$
Cell dimensions				
<i>a</i> , <i>b</i> , <i>c</i> (Å)	49.98, 49.98, 118.68	120.67, 120.67, 85.51	78.59, 82.56, 81.43	116.546, 116.546, 223.384
$\alpha$ , $\beta$ , $\gamma$ (°)	90.0, 90.0, 120.0	90.0, 90.0, 120.0	90.0, 102.2, 90.0	90, 90, 120
Resolution (Å)	40.66–2.2 (2.25–2.2)	45–2.2 (2.75–2.2)	100–2.3 (2.34–2.3)	46–1.65 (1.75–1.65)
<i>R</i> sym	0.09 (0.617)	0.156 (0.76)	0.15 (0.765)	0.06 (0.34)
<i>I</i> / $\sigma$ ( <i>I</i> )	6.3 (3.4)	16.2 (3.1)	7.6 (1.3)	16.45 (3.38)
Completeness (%)	100 (99.9)	100 (100)	97.4 (95.4)	97.2 (85.1)
Redundancy	25.1 (19.2)	40.8 (33.2)	5 (4.5)	7.29 (4.64)
<b>Refinement</b>				
Resolution (Å)	40.66–2.2	44.6–2.2	39.8–2.3	33.6–1.65
No. reflections	4758	19,136	44,127	68,087
<i>R</i> <sub>work</sub> / <i>R</i> <sub>free</sub>	28.4/32.3	21.3/24.7	23.2/29.3	19.4/22.5
No. atoms				
Protein	596	1772	7297	3553
Solvent	14	119	31	250
<i>B</i> factors average (Å <sup>2</sup> )	60	44	37	25
R.m.s. deviations				
Bond lengths (Å)	0.01	0.01	0.01	0.01
Bond angles (°)	1.3	0.89	1.03	0.89

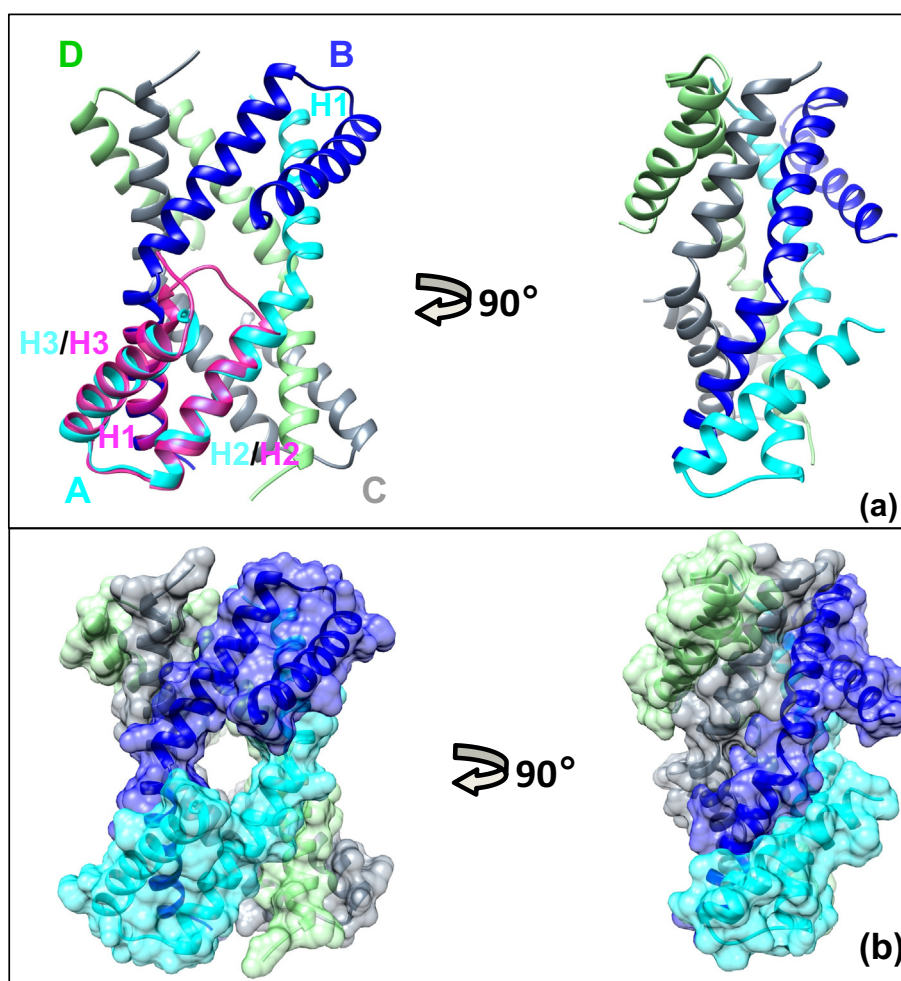


**Figure 1.** Crystal structure of sRI (PDB = 6PSH). (a) Ribbon diagram of tetramer observed in the crystal of the free sRI, colored by subunit: cyan, subunit A; blue, subunit B; gray, subunit C; and light green, subunit D. H1–3 helices are marked for the subunit A in corresponding color. The domain swapped conformation of RI when bound to sT is illustrated in the overlay of sT-bound sRI (magenta) with subunit A of free sRI, H1–3 helices are labeled for this form in magenta. (b) Two views of the surface representation of the sRI tetramer, colored by subunit same as in (a), illustrate extensive contacts among subunits.

helix with a slight bend. It actually has a single amino acid residue, Phe45, that is not in an  $\alpha$ -helical conformation, which causes a bend of about  $15^\circ$  between H1 and H2. The H2-helix is connected to H3 (residues 72–92) through a hairpin loop, which is linked to the H3-helix by a disulfide bond between Cys69 and Cys75. The structure of RI is unique, based on searches of the PDB database by the vector alignment search tool (VAST) [14]. Only two hits are identified by VAST, with low similarity scores of 3.6 and 3.7 ( $P$  values of 0.0105 and 0.0139). In both cases, the aligned regions correspond to isolated  $\alpha$ -helices of larger proteins.

Although the asymmetric unit of the crystal contains a single RI subunit, the crystal lattice clearly shows that RI is a homotetramer formed by the  $C2$  space

group symmetry, where the AB pair of subunits is equivalent to the CD pair (Figure 1). The total surface area of the tetramer calculated by PDBePISA [15] is  $15,006.7 \text{ \AA}^2$ , with a total solvent-accessible surface area buried by the tetramer formation of  $8618.8 \text{ \AA}^2$  representing a significant portion of a total surface. The PDBePISA solvation free energy gain ( $\Delta G^{int}$ ) upon formation of the tetramer is estimated at  $-87 \text{ kcal/mol}$ , with the negative value indicating a large contribution of hydrophobic interactions at the interface. The calculated free energy for the tetramer dissociation ( $\Delta G^{diss}$ ) of  $13.8 \text{ kcal/mol}$ , with the positive value indicating that this tetramer is thermodynamically stable. The tetramer is maintained through three distinct interfaces (Figure 1), with the majority of contacts at the interface between subunits A and B

(equivalent to C and D) and at the interface between subunits A and D (equivalent to B and C). The  $\Delta^1G$  values, buried area, and the list of contacts for each interface are listed in Supplementary Table 1.

For the AB (equivalent to CD) interface, sRI packs in a head-to-tail fashion, where  $\alpha$ -helices H2 and H3 comprise the head, and H1 forms the tail (Figure 1). The tail of one subunit packs onto the head of another subunit in a groove between helices H2 and H3. The AB interface involves over 50 contacts, including 10 hydrogen bonds contributing to the interactions (S. Table 1). The AD (equivalent to CB) interface is made by the long kinked  $\alpha$ -helices (H1–H2) of one subunit running antiparallel with the H1–H2 region of the adjacent subunit (Figure 1), with the six hydrogen bonds and two salt-bridges (S. Table 1) in addition to multiple hydrophobic and van der Waals contacts. The path for dissociation of the tetrameric assembly of sRI, as predicted by PDBePISA based on the lowest free energy, starts with breaking into two dimers (AB and CD). Previously, analysis with size exclusion chromatography showed that sRI was predominantly a monomer [6] with a small fraction in a dimer state. Moreover, analytical centrifugation results also showed a monomer. However, in these studies, the highest concentration probed was 1.6 mg/ml, which is much lower than the concentration used for crystallization (10 mg/ml). Our current interpretation is that oligomeric state of sRI is concentration-dependent. It can exist as compact monomer while at low concentration and go into higher oligomeric states (dimer and tetramer) at a higher concentration.

### The periplasmic domain of the T holin forms a heterotetrameric complex with the periplasmic domain of the RI antiholin

To understand how the antiholin binds and inhibits T, we solved the structure of the sRI–sT complex. We have previously shown that sT forms a complex with purified sRI [6]. The two proteins co-eluted as a complex from a size exclusion column. The complex was crystallized in the  $P6_522$  space group crystals with one sRI–sT dimer in the asymmetric unit. The initial phases were determined by SAD with the complex formed between selenomethionine-modified sRI and sT. The structure of the complex was refined using diffraction data to 2.2 Å resolution, with an  $R_{work}$  of 21.3, an  $R_{free}$  of 24.7% and good stereochemistry. The final model of the complex covers sT residues 78–218 and sRI residues 25–95 (no density was observed for sT residues 56–77 or for 96–97 of sRI). The data collection and refinement statistics are summarized in Table 1. Although the asymmetric unit of the  $P6_522$  crystals contained a single sRI–sT complex, a heterotetramer was clearly visible in the lattice (Figure 2(a)). Analysis by PDBePISA [15] indicates that this heterotetramer is thermodynamically stable, with a negative solvation

free energy gain ( $\Delta G^{int}$ ) of  $-24.5$  kcal/mol signifying hydrophobic interface, positive free energy for tetramer dissociation ( $\Delta G^{diss}$ ) of 13 kcal/mol, and a suggested dissociation pattern of 2(RI–T). The total surface area of the tetramer is  $18,878 \text{ \AA}^2$ , with the area buried in all interfaces of the assembly being  $5550.3 \text{ \AA}^2$ , almost 30% of the total surface. The data on oligomeric state in the solution obtained by size exclusion chromatography [6] were ambiguous, with the major peak calculated at 45.6 kDa, a mass larger than a calculated mass for a dimer (29.7 kDa) but smaller than a tetramer (59.4 kDa). The conclusion was made based on the analytical centrifugation data that sRI–sT complex is a dimer. However, seeing in the structure how compact the heterotetramer is and taking into account that S75 column is not optimal for resolving proteins with the size closer to 60 kDa, we believe that previously obtained data are also consistent with the compact tetrameric form of sRI–sT complex in solution.

In contrast to the tetrameric structure of the free sRI, sRI engages in contact with sT as a single subunit. The transition from the tetrameric state of sRI to the monomer is accomplished by a major rearrangement of the H1-helix, highlighted by a  $\sim 19 \text{ \AA}$  movement of closest to the hinge end of H1 (Leu44) and  $\sim 54 \text{ \AA}$  translocation of the other end of H1 at Pro28 so that it directly packs against H2 and H3 of the same molecule. Remarkably, with this large change from the elongated to compact form, the main-chain conformational changes are restricted to a short region including Phe45 that separates H1 and H2, as described above (Figures 1(a), 2(a)). The region encompassing residues 44–49 acts as a hinge and undergoes a conversion from the  $\alpha$ -helix in the free sRI into a loop in the sRI–sT complex. This hinge allows the dramatic movement of the H1 helix (Figure 1(a)) from a nearly co-linear position with H2 to becoming anti-parallel to it. In the free sRI structure, the H2–H3 helices form a groove that accommodates H1 from the other subunit, whereas in the T-bound single subunit form, this groove between H2 and H3 binds the H1 helix from the same subunit so that it can form the same interactions without a second subunit. This rearrangement is known as “domain swapping” [16].

Domain swapping occurs when higher-order oligomers are made through the exchange of identical domains. Through this process, the same contact interface is maintained, with large changes restricted to the transitioning hinge region. The overall impact of sRI converting from its elongated form into a compact monomer is that it can bind to sT. The H1–H2 surface of the monomer becomes the interface for binding two molecules of sT in a heterotetramer. Each sRI subunit forms both hydrogen bonds and van der Waals interactions with two sT molecules (details are listed in Supplementary Table 2), with sRI–sT interfaces 1 and 2 providing the majority of buried surface area and contacts (PDBePISA [15]).



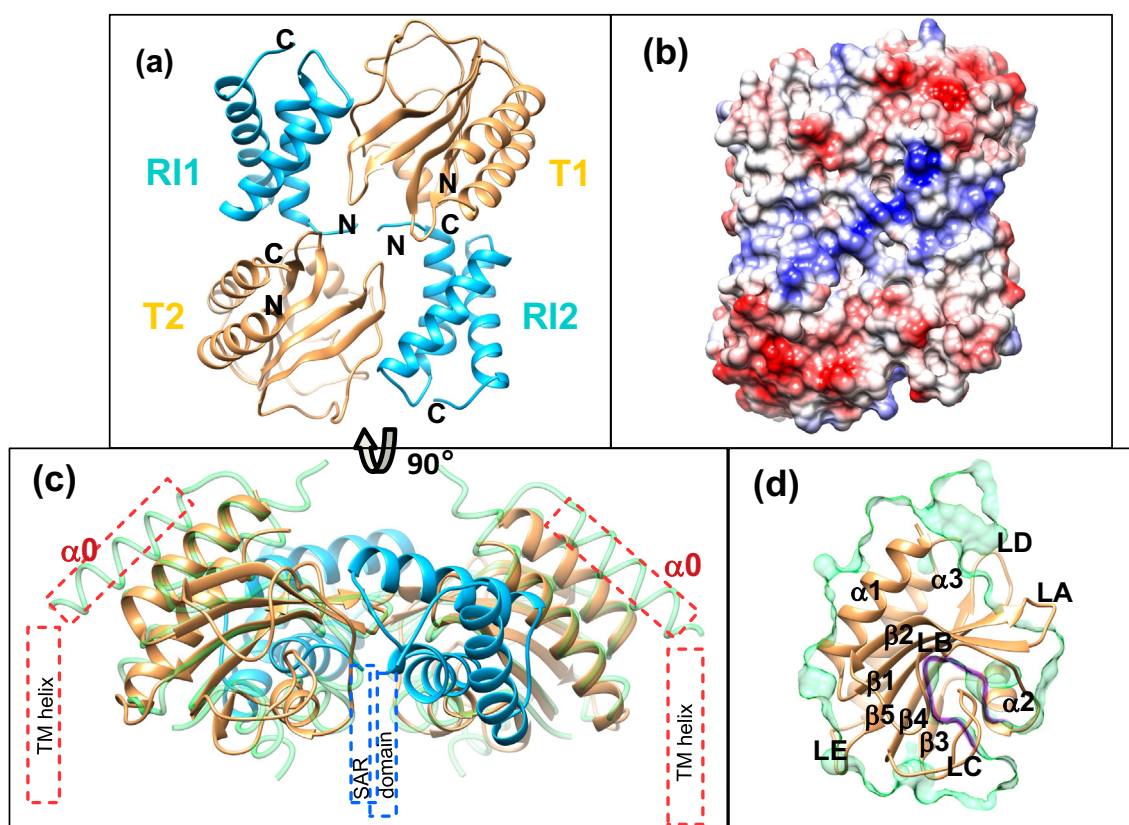


**Figure 2.** Crystal structure of sRI-sT complex (PDB = 6PSK, 6PXE). (a) Ribbon diagram of hetero-tetramer observed in crystals of the sRI-sT complex. sRI subunits are colored in light blue and sT in tan. (b) Surface representation of the sRI-sT complex colored by electrostatic potential; the orientation is the same as in (a). (c) 90° rotated view of the sRI-sT complex depicted in (a). GAF domain homolog structure (pdb ID: 2ool) shown as green licorice ribbon is superimposed on both sT subunits for a comparison. Putative positions for the elements not covered by the crystal structure are shown as dash outlined boxes: blue for the SAR domains of RI, and red for the transmembrane (TM) helix and  $\alpha 0$  of T. (d) Elements of the structure are marked on the ribbon representation of the sRI bound form of the sT. Clipped surface view of the overlaid GAF domain homolog structure (pdb ID: 2ool) is shown in green to illustrate that LC loop of sT blocks putative GAF pocket (highlighted by purple line).

Residues from the H1 and H2  $\alpha$ -helices of sRI are involved in interactions primarily with the  $\beta 1$ -LA- $\beta 2$  region and the LB loop region of the sT subunit (Figure 2(a) and (d)). Twenty-one hydrogen bonds and five salt-bridges stabilizing the 2sRI-2sT complex are listed in S. Table 2. Collectively, these extensive interactions result in the heterotetrameric complex that is very stable in solution. The heterotetramer is unlikely to be due to a crystallization artifact as the same assembly was observed in all multiple crystal forms (Table 1), and it is what we observe in the cryo-EM structure described below. Using differential scanning fluorimetry, we found that the complex shows a single transition melting curve with a  $T_m$  of approximately 55 °C signifying that the solution sample is all in one form of a tight cooperatively melting complex. All those observations are inconsistent with the current view that RI needs to be activated/stabilized by LIN signal in

order to engage with T, and prompted us to re-examine the model.

### The overall structure of the periplasmic domain of the T holin

The sT structure comprises a central twisted antiparallel five-stranded  $\beta$ -sheet formed by the  $\beta 1$ - $\beta 5$  strands, flanked by two  $\alpha$ -helices on one side of this sheet (an N-terminal  $\alpha 1$ -helix and a C-terminal  $\alpha 3$ -helix), and loops and a short  $\alpha$ -helix ( $\alpha 2$ ) on the opposite side (Figure 2(d)). An intrasubunit disulfide bond links Cys175 of the  $\beta 4$ -strand with Cys207 of the  $\alpha 3$ -helix C-terminal.

A structural similarity search of sT using both VAST [14] and DALI [17] revealed unexpected matches to several GAF domain proteins (cGMP-specific phosphodiesterases (PDEs), *Anabaena* adenyl cyclases, and *E. coli* FhlA proteins), with

structural similarity scores ranging from 10 to 12.7. GAF domains are involved in oligomerization regulated by the binding of a ligand in hundreds of regulatory proteins, as well as similar to it PAS (Per, Arnt, Sim) domain of sensory and signaling pathways. While GAF/PAS domains have been shown to interact with a diverse set of small molecule regulators, the ligands for many of these proteins remain unknown. The GAF domain closest to sT with a VAST score of 12.7 at 12.6% sequence identity (PDB: 3W1T) has no ligand bound. The closest structure with ligand (PDB:1MC0, VAST score = 12.6 at 11.8% sequence identity) has a cyclic GMP bound in the small-molecule binding pocket between the central  $\beta$ -sheet and surface loops/short helix. This site maps to the sT holin structure between the central  $\beta$ -sheet, loops LB- $\alpha$ 2, and LC, with the potential for loops LB- $\alpha$ 2 and LC to rearrange and position residues Glu141, His145, Asp136, Phe159, and Tyr191 to line the pocket. However, in the sT-sRI complex structure this pocket is buried, blocked by the LC loop (Figure 2(d)).

The region directly following the TM-helix of T (residues 56–78) does not have well defined electron density. Although these residues are predicted to form an  $\alpha$ -helix ( $\alpha$ 0), the electron density of this region was missing in nearly all sRI-sT complex data sets. One of the two tetramers in the asymmetric unit in crystal structure in *P2<sub>1</sub>* had density for amino acids 62–78 of  $\alpha$ 0. It is likely that without the transmembrane helix and the membrane to support it, the  $\alpha$ 0 position is disordered. We observed well-ordered electron density beginning with Phe79 of the following  $\alpha$ -helix ( $\alpha$ 1). The position of  $\alpha$ 0 anti-parallel to  $\alpha$ 1 (Figure 2(c)) was modeled based on homology to other GAF domain proteins. This placement is consistent with the membrane topology as determined by the position of the sRI N termini in the complex structure followed by the membrane-embedded SAR domains.

### Single-particle cryo-EM of the sRI-sT complex

To verify that the sRI-sT heterotetramer exists in solution, we subjected the purified sRI-T complex to cryo-electron microscopy. Although the size of a single heterotetramer was below the detection limit, we were able to pick 35,432 larger particles from the Cryo-EM grid. After 3D reconstruction, a density map was generated at 9.4 Å resolution. The structure of the sRI-sT complex from the *P2<sub>1</sub>* crystal (PDB = 6PXE) was used to fit and refine into the density map. The density of the observed particles was fully accounted for by four sRI-sT heterotetramers (Figure 3). The heterotetramers in the assembly observed in cryo-EM are mainly interacting through sRI H3 and  $\alpha$ 1 of sT, with the  $\alpha$ 0 regions (residues 55–77) bundling in the middle of the assembly (Figure 3). The assembly of the heterotetramers resembles the organization of the

heterotetramers in the lattice of *P6<sub>522</sub>* crystals and is unlikely to be physiologically relevant. Nevertheless, these results validate the existence of the heterotetramer in solution and perhaps indicate the propensity of  $\alpha$ 0 to self-interact.

### The holin-antiholin complex binds dsDNA

Our data suggest that RI-T complex is pre-formed in the infected cell, and therefore the establishment of LIN under condition of a superinfecting phage would stabilize the RI-T complex as an inhibited form of T and prevent the formation of a membrane hole.

We next looked at likely candidate molecules that would stabilize the complex. Since other T4-like phages including T2 and T6 can induce LIN in T4-infections but have different internal protein molecules [18,19], we hypothesized that the signal molecule was the gDNA. It has been shown that DNA of the superinfecting phage is trapped and degraded in the *E. coli* periplasm [13]. Since the holin-antiholin complex would need to sense any degradation products of the gDNA, we reasoned that the binding to the complex would not likely be sequence-specific. To test this, we first performed pilot mobility shift assays with three nucleic acids of different length and sequences and the purified sRI-sT complex. We observed that three DNA molecules, including single stranded (ss) 70 bp, double-stranded (ds) 30 bp, and ds 58 bp species, were all shifted by the sRI-sT complex in a protein concentration-dependent manner to a position where Coomassie staining shows the protein band (Figure 4). In contrast, purified sRI alone did not cause these molecules to shift (data not shown). To assess the relative affinity, we determined the apparent  $K_d$  values using intrinsic fluorescence quenching. The results, summarized in Table 4, show that the sRI-sT complex binds a wide variety of nucleic acids, including double- and single-stranded DNA and RNA fragments, with no identifiable sequence specificity. The sRI-sT complex also binds deoxyribonucleotides, tri-, di-, and monophosphate nucleotides. Binding was driven more by the nucleoside moiety than by phosphate groups, as guanosine has a lower  $K_d$  (43  $\mu$ M) than AMP (72.4  $\mu$ M) or ADP (213.6  $\mu$ M), and 5-phosphorylribose-1-pyrophosphate has a relatively high  $K_d$  of 225.9  $\mu$ M.

### Discussion

The LIN phenomenon was documented in the first experiments of modern molecular genetics and has been the subject of many genetic and physiological studies [11]. Clever experiments have been devised and implemented to figure out the proteins and their functional connections, as reviewed by Abedon [20]. However, the molecular mechanism of lysis and lysis

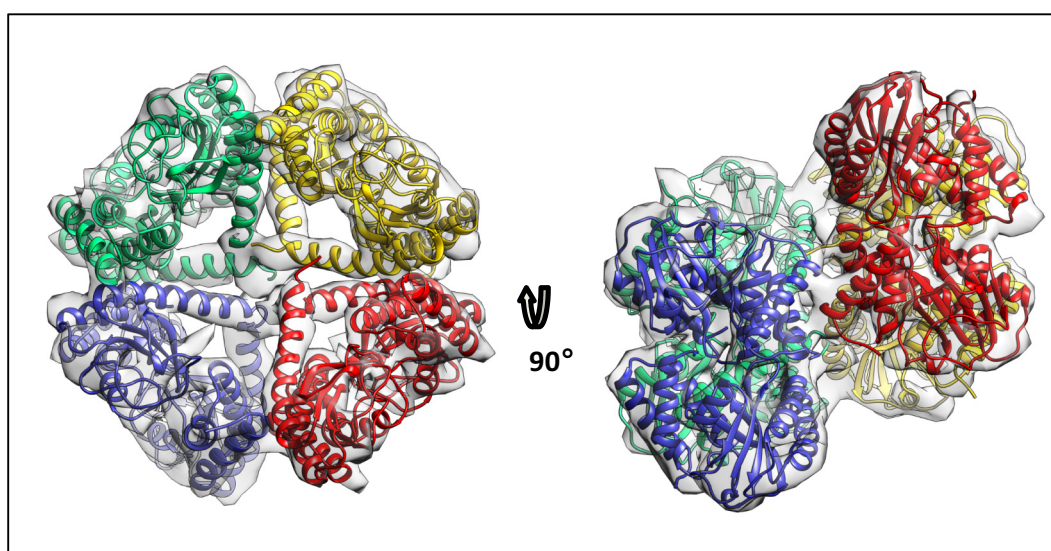


**Figure 3.** Cryo-EM structure of sRI-sT heterotetramers in solution. Crystal structure of sRI-sT complex from the *P2<sub>7</sub>* crystal (PDB = 6PXE) with the longest residue coverage was used to fit and refine into the EM density resulting in the assembly of four sRI-sT heterotetramers (colored by tetramer). The EM density is deposited under EMD-22250 EMDB ID.

inhibition in T4 phage has remained obscure with the lack of structural information and no homology to holins and antiholins of other characterized phages [4]. The most recent model [8] proposed that the antiholin RI plays no role in normal lysis timing; instead, in the absence of a superinfection, RI is synthesized, secreted to the periplasm, and then rapidly degraded. It is only when RI is stabilized by an unknown signal generated by a superinfection

event that it accumulates sufficiently to bind to the periplasmic domain of the T holin and to block progression in the hole-formation pathway.

The sRI2-sT2 heterotetramer structure analysis enabled us to propose a new model with additional mechanistic insights. Our data clearly point to the formation of the heterotetrameric RI-T complex as an early step in the normal pathway for T-mediated lysis. The position of the N-proximal helix of sRI in the

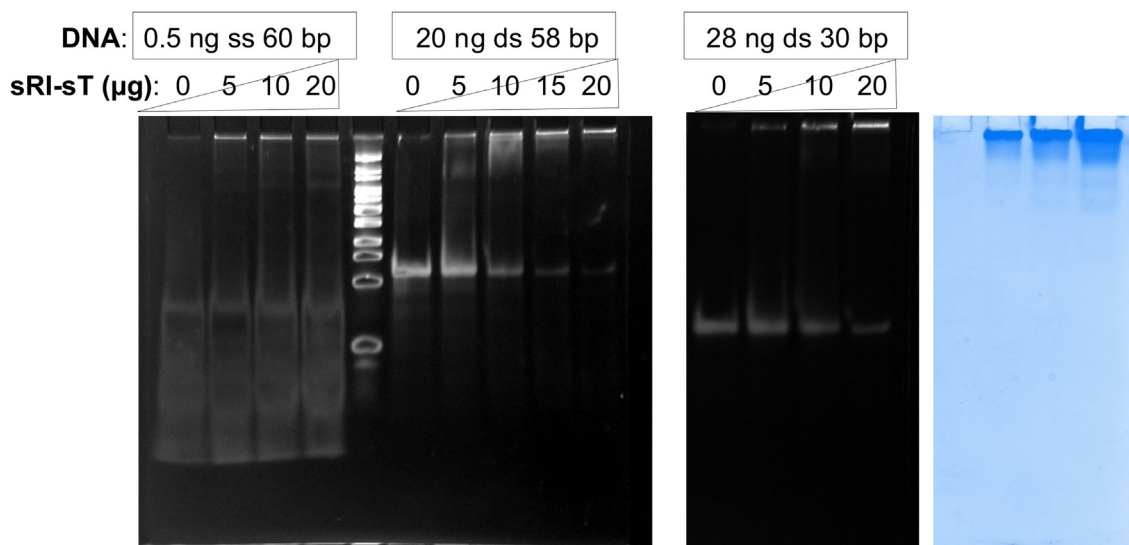


**Figure 4.** Binding of sRI-sT complex to DNA tested by electrophoretic mobility shift assays. DNA was separated in acrylamide gel in the absence or in the presence of various amounts of sRI-sT protein complex. The first two panels are stained for DNA by gel green, and the last panel shows the same gel (for 30 bp DNA) stained with Coomassie to visualize the protein.



**Table 4.** RI–T complex binds dsDNA

Ligand	$K_d$ ( $\mu$ M)
58 bp ds DNA	0.04
30 bp ds DNA	0.29
21 bp ds DNA	0.36
70 bp ss DNA	1
20 bp RNA	6.1
dNTP mixture	30.2
dATP	18.9
AMP	72.4
ADP	213.6
Guanosine	43
5-Phosphorylribose-1-pyrophosphate	255.9
Phosphate	18,600

Apparent  $K_d$  values obtained by intrinsic fluorescence quenching.

heterotetramer is important as it determines the position of the membrane within which the RI SAR domain is embedded (Figure 2(c)). This argues that newly exported membrane-tethered RI forms complexes with T. Since RI is expressed in both early and late transcriptional phases whereas T is a late protein [21], there are membrane-tethered RI molecules present before the first T molecules appear, sequestering the T holin to prevent premature lysis. From this perspective, the stability of the sRI:sT complex presents a conceptual problem: what allows T to be liberated to pursue oligomerization and hole formation? Before T begins to accumulate at the start of late gene expression, the level of membrane-tethered RI available for complex formation would be limited by the metastable integration of the SAR domains in the bilayer and its recognition by DegP in the periplasm, which results in RI degradation [9]. The simple view of lysis triggering is that T, which is proteolytically stable and invariably membrane tethered, eventually titrates out the supply of RI. The accumulation of free T would then follow the familiar pathway of reaching a critical concentration, followed by formation of holin oligomers [22] that depolarize the membrane. It has been established that SAR domains exit the membrane quantitatively after depolarization [23], suggesting that it is the exit of the N-terminal SAR domain of RI from the bilayer that disrupts the RI–T complex and results in release of the T proteins from inhibition. Thus, at the instant of holin triggering, many T molecules are liberated from antiholin-inhibited complexes to participate in the formation of holes in the membrane. The structure of the free sRI suggests that after simultaneous dissociation from the T holin, locally concentrated RI likely forms a domain-swapped homotetramer that would no longer be competent to bind T, making T activation irreversible. When probed by size exclusion chromatography in the solution, only small fraction of sRI shows in the oligomer state. It is likely that the tetrameric state is assumed at a higher concentration of the protein than can be maintained during gel filtration. Physiologically, high local concentration of RI would be

achieved at the moment of lysis triggering, when all RI molecules are simultaneously released from the RI–T complexes. The major conformational change between the free and holin-bound forms of RI is localized to a short “hinge” region, in a similar way to other proteins like hemagglutinin and cystatin E where domain swapping is shown to regulate their function [24] [25]. In hemagglutinin, the loop-to-helix transition of the hinge region is thought to be driven by the change of solvent accessibility of this region [26]. When lysis begins, the SAR release from the membrane and dissociation of RI from T may expose the hinge region and, analogously to hemagglutinin, induce the loop-to-helix transition that causes RI to assume an elongated form prone to oligomerization.

Functionally similar participation of antiholins in lysis occurs with both the canonical lambda holin and the phage 21 pinholin [27] [28]. In both cases, the antiholin is an alternate translational product of the holin gene, and in both cases, the distinction between the otherwise identical proteins is that the topology of the N-terminal transmembrane domain of the antiholin is constrained by the energized membrane. Much of the holin accumulates in inhibited complexes and thus cannot participate in the mass action required for lysis. However, at the instant of triggering, the antiholins are converted to the holin conformation in response to membrane depolarization, and both gene products are able to participate in hole formation. The mechanism we are proposing for T4 phage is molecularly distinct but conceptually similar to these systems. In all three cases, the antiholin functions to amplify holin hole-formation kinetics without allowing excess holin supply to cause premature lysis. Our model for the role of RI in the normal lysis pathway predicts that in the absence of RI, lysis timing would be accelerated. Indeed, earlier lysis was observed for the *r48* LIN-defective allele of *rl* [21].

The T4 holin architecture is distinctly different from the other holins, which are dominated by transmembrane domains. This poses another mechanistic puzzle: how does the T holin assemble into a hole to line a membrane with a single transmembrane helix despite being constrained by a relatively large periplasmic domain? This issue is problematic to address by direct experiments: the full-length, self-assembling, membrane-integrated holin constitutes a difficult subject for structural studies. Even truncated sT is prone to aggregation and not soluble on its own [6]. However, the GAF domain structure of the inhibited form of sT provides us with clues as to how hole formation may occur. GAF domains are known to oligomerize after undergoing a conformational change associated with ligand binding in a pocket on the face of the molecule opposite to the  $\alpha$ -helices that engage in self-interactions. Ligand binding leads to change in the relative position of the  $\alpha$ -helices, enabling oligomerization. In the sRI–sT complex, the putative ligand pocket is blocked by



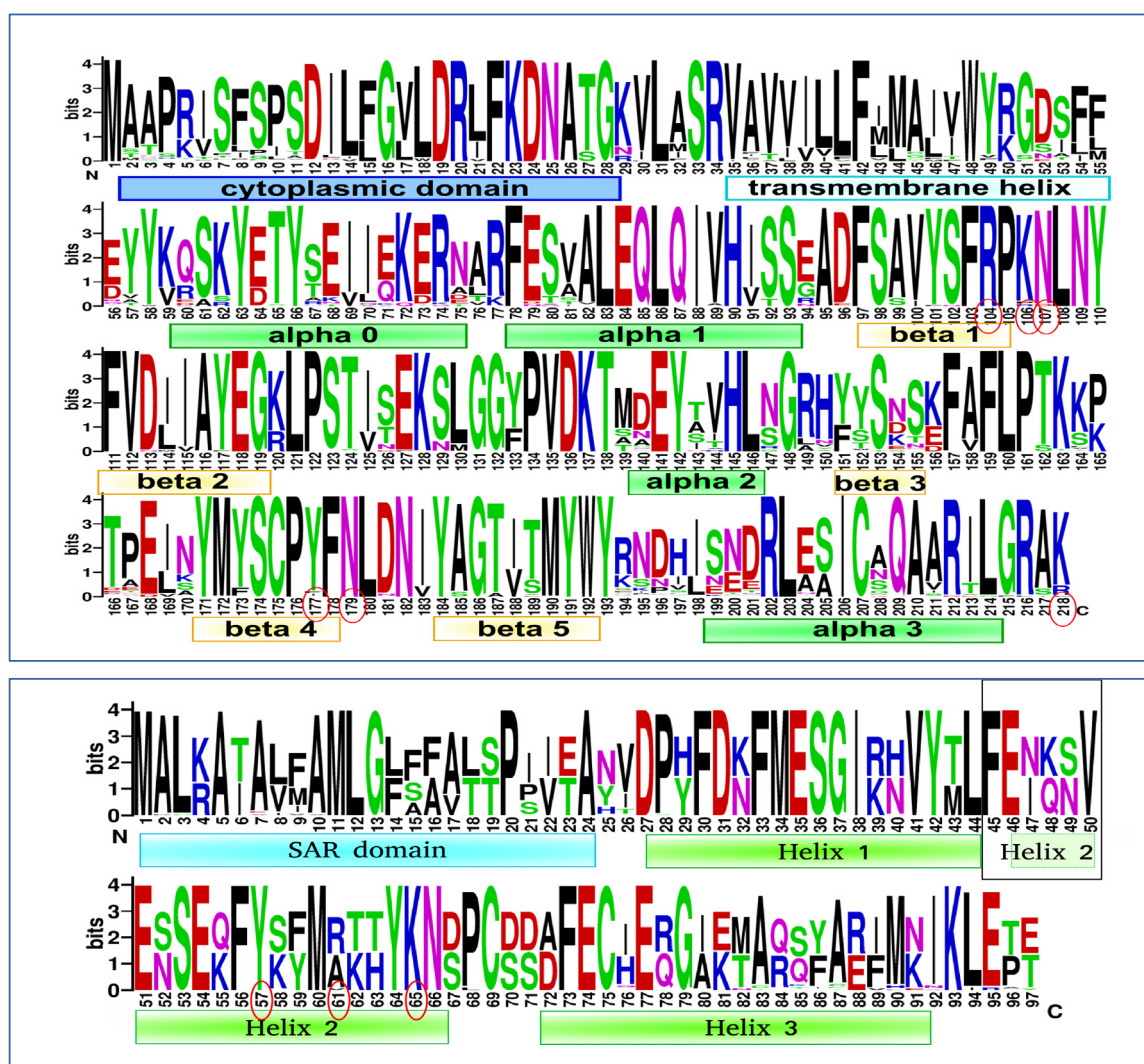


**Figure 5.** Conservation level across the sequences. The overall height of the stack indicates the sequence conservation at that position, while the height of symbols within the stack indicates the relative frequency of each amino acid at that position. The secondary structure elements marked as boxes and the residues potentially interacting with DNA circled in red. (a) Holin T, constructed based on 100 BLAST hits from phages of *Escherichia*, *Shigella*, *Yersinia*, *Salmonella enterica*, *Pseudomonas*, *Citrobacter*, *Klebsiella*, and *Acinetobacter*. (b) Antiholin RI, constructed based on 47 top BLAST hits from phages of *Escherichia*, *Shigella*, *Yersinia*, and *Salmonella enterica*. Loop-to-helix conformation changing region is boxed. The figure was created with WebLogo.

the T holin LC loop, which, both directly and through the LB- $\alpha 2$  region, interacts with sRI (Figure 2(c, d)). Based on the inherent GAF domain properties, it is reasonable to expect that when the complex dissociates upon lysis triggering, the LC loop may move out of the ligand binding site of T, causing a conformational change in the helix positions that will favor T oligomerization and hole formation. It is interesting to note that out of five selected mutations of T holin incapable of lysis inhibition by RI but still competent for lysis, four map to the regions contributing to blocking the GAF pocket Thr138Ala, Ser153Phe, Ser153Pro, and Ala158Ser [3]. In another study that selected for lysis-defective

mutants of T holin [29], four mutants were incapable of interaction with RI, with only one mutated residue involved in direct contact to the RI interface (Phe111Ser), while the others mapped to either the LB loop (Lys137Arg) or to the  $\alpha$ -helices (Ile88Lys and Ile213Lys).

As noted above, a long-standing issue about LIN is the identity of the signal that comes from the superinfecting virion. The observation that "ghost" phage particles emptied of the capsid contents are unable to induce LIN led to a hypothesis that the 170 kb gDNA of the superinfecting phage, ectopically localized to the periplasm, may play a role [21] [20]. The periplasm is rich in nuclease activity [30] so the 170 kb gDNA is

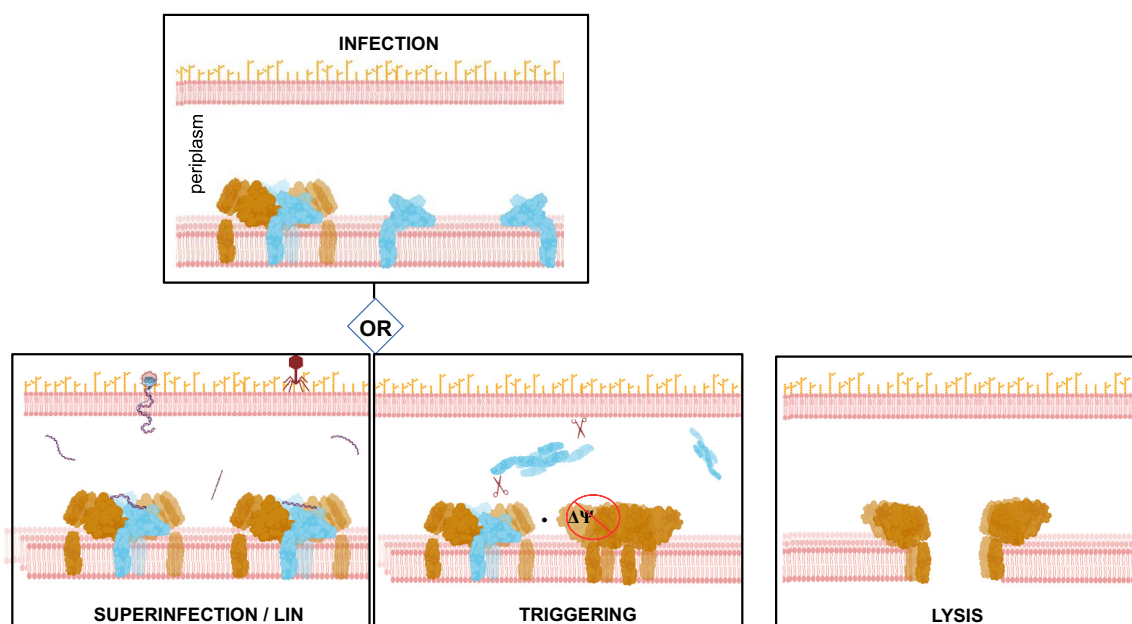


**Figure 6.** Model of lysis timing control in T4 phage. Holin molecules depicted in brown and antiholin in light blue. Periplasmic protease DegP marked as scissors. The figure was created with [Biorender.com](https://biorender.com)

likely to be degraded into smaller fragments very rapidly upon its ejection. A single gDNA could generate >3000 50-bp fragments upon partial nucleolytic degradation, corresponding to a periplasmic concentration of  $\sim 30 \mu\text{M}$ , which is comparable with the range of  $K_d$  values we observed for nucleic acids binding to the holin–antiholin complex. This is consistent with the observation that a single superinfecting phage can induce LIN [31]. Moreover, in any scenario where a single superinfection occurs, subsequent superinfection events are likely to happen, which would increase the DNA concentration and thus further enhance the LIN state. Here we provide direct evidence that phage DNA and its fragments can serve as the superinfection signal sensed by the holin–antiholin complex. We observed that the sRI–sT complex binds DNA in a sequence-unspecific fashion with low nanomolar to low micromolar affinities *in vitro*, while the free sRI shows no DNA binding. The sRI–sT complex structure does not display any obvious DNA binding domains, like helix–turn–helix, leucine zipper, and other motifs observed in DNA regulating proteins. Since it is not designed to recognize a defined DNA sequence, the holin–antiholin case is more similar to a general DNA sensing protein, like the innate immunity protein cGAS, which displays large positively charged patches on its accessible surface. Analysis of the electrostatic surface of the sRI–sT complex crystal structure identified only one positively charged patch consistent with potential DNA binding (Figure 2(b)). This patch is located on the face opposite to the sRI N termini protrusion and thus would face the periplasm. All four protein chains making the sRI–sT heterotetramer contribute to this positively charged patch,

suggesting that DNA binding could stabilize the RI–T heterotetrameric complex. The residues potentially interacting with DNA (Lys106, Lys218, Arg104, Asn107, Asn179, Tyr177 of T, and Lys65, Arg61, Tyr57 of RI) are reasonably conserved (Figure 5) and repeated on that surface twice because of the heterotetramer symmetry. Based on this conservation, T4-like phages infecting a wide range of Proteobacteria can be identified that are predicted to be capable of the LIN response (Figure 5).

The stabilization derived from DNA binding would need to be subverted once triggering occurs; destabilization would most likely be driven by the collapse of the membrane potential once the concentration of DNA in the periplasm decreases due to continuous nucleolytic degradation. Indeed, LIN can be collapsed at any time by membrane depolarization with energy poisons [7]. Depolarization would release the SAR domains of RI from the bilayer [23] disrupting the holin–antiholin complex and rendering moot the presence of the DNA signal.

T4 LIN has been the subject of extensive genetic and physiological study for over seven decades, since the *rl* gene was among the first heritable genetic markers identified in phage [32]. The structural studies here, along with details of the interaction between the periplasmic domains of the holin and antiholin and the domain-swapping transition that underlies the inactivation of RI, provide a molecular basis for the function of this remarkable system. Our proposed model of lysis timing control in T4 phage is depicted in Figure 6. Moreover, we have provided biochemical evidence that T4 DNA itself is the long-sought LIN signal; to our

knowledge, this is the first example of DNA acting as a physiological signal molecule. Studies aimed at testing the model, including using alternative pathways to introduce DNA into the periplasm of the T4-infected cell, are underway.

## Methods

### Crystallization of sRI and the sRI–sT complex

The periplasmic domain sRI of RI (residues 25–97) with C-terminal histidine tag was purified as reported previously [6]. Crystals were obtained at 16 °C by hanging-drop vapor diffusion in 100 mM Na citrate (pH 4.5), 1 M Na acetate, 0.5% Anapoe X114 detergent and flash-frozen in the reservoir solution with 24% ethylene glycol. The Se-Met-labeled derivative of sRI was prepared, purified, and crystallized similarly.

The periplasmic domain of the T4 holin T (sT, residues 56–218) was expressed as either tagless or C-terminally histidine tagged version. For the initial crystal screening and Se-Met-labeled crystals, sRI–sT complex was obtained and purified following procedures in [6]. After the phase was solved, additional crystal forms were explored using tagless sT. In these experiments, a simplified procedure was used in which sRI–sT complex was formed upon co-lyzing mixture of two cultures, one expressing tagged sRI and the other the tagless sT. The complex was then purified on Ni affinity column, followed by gel filtration. Crystals of Se-Met complex were obtained at 16 °C by hanging-drop vapor diffusion by mixing 10 mg/ml protein in 20 mM phosphate (pH 8.0) and 100 mM NaCl with 1.0 M ammonium sulfate, 0.1 M Bis–Tris (pH 5.5), and 1% PEG 3350. Native complex *P6<sub>522</sub>* crystals were grown in 3.2 M NaCl and 0.1 M Na acetate trihydrate, pH 4.6 condition; native *P2<sub>7</sub>* crystals formed in 25% PEG 3350 with 0.1 M citric acid (pH 3.5). Higher resolution crystals (in *H3<sub>2</sub>*) were obtained using shorter version of sT (residues 78–218) for the sT–sRI complex formation in 0.8 M Na/K Tartrate and 0.1 M Tris–HCl (pH 7.0–8.0).

### Structure determination

X-ray diffraction data were collected at 100K on beamlines 19-ID and 23-ID at APS (Argonne National Labs, Chicago, IL) at Se edge wavelength. Diffraction data were processed using HKL2000 [33]. The structure of sRI was obtained by the SAD method using a crystal of the Se-Met substituted protein and data at 2.5 Å resolution. All six potential Se sites were located using SHELXD [34], with their positions refined and the phase solved by SHARP [35]. Automated model building was performed using

the PHENIX suite [36]. The residual 26% of the model was built manually using COOT [37] and refined with PHENIX using native crystal data with higher resolution diffraction.

sRI–sT complex structure was similarly solved by SAD with the data from Se-Met substituted protein crystal. Diffraction data were processed using HKL2000 [33]. Automated structure solution was carried out by the PHENIX AutoSol wizard resulting in preliminary model. This model of sRI–sT was rebuilt by PHENIX AutoBuild. The model was further manually built using COOT and refined by PHENIX Refine. Two alternative space-group data sets for sRI–sT complex crystals (*P2<sub>1</sub>* and *R3<sub>2</sub>*) were integrated and scaled using the PROTEUM software suite [38], with the data subsequently truncated with Ctruncate from CCP4 [39]. The structures were solved by molecular replacement using Molrep [40] from CCP4 and sRI–sT heterodimer structure obtained from the Se-Met phasing as a search model. Subsequent model improvement and refinement was done using PHENIX Refine and COOT iteratively. Data collection and refinement statistics are provided in Table 1.

### Single-particle cryo-EM imaging

Three microliters of the sRI–sT specimen (0.1 mg/ml) was applied to a C-Flat 1.2/1.3 holey carbon grid at room temperature with 100% relative humidity and vitrified using a Vitrobot Mark III (FEI). The prepared grids were imaged under an FEI Tecnai F20 transmission electron microscope operated at 200 kV. Data were recorded on a Gatan K2 Summit with electron-counting mode. A nominal magnification of 25,000× was used, yielding a pixel size of 1.5 Å. The beam intensity was adjusted to the dose rate of ~10 e<sup>−</sup>/pixel/s on the camera. A 40-frame movie stack was recorded for each picture, with 0.2-s per frame, for a total exposure time of 8 s.

### Cryo-EM image processing and model building

Five hundred eight collected image stacks were aligned and filtered based on the electron dose using Unblur [41]. The defocus value of each image stack was determined by Gctf [42]. Particles were semi-automatically picked using the Erase and Swarm tools of e2boxer.py in EMAN2 [43]. In total, 139,834 particles were picked with a box size of 144 × 144 pixels. The 2D and 3D classifications were performed using Relion [44] to get clean and homogeneous particles for the final 3D reconstruction. After the post-processing, the final refined map from 35,432 particles yielded a resolution of 9.4 Å. The particle images were downsampled by 2-fold in all processing procedures. Refinement using the particles without downscaling did not improve the resolution of the refined map. To build the model,



the crystal structure of the sRI–sT tetramer was first fit into the EM density. In total, the EM map can accommodate four tetramers. To have a better fitting, the initial model of the four tetramers was then refined using the molecular dynamics flexible fitting with secondary structure restraints [45].

## DNA binding

For these experiments the sRI–sT complex was purified and stored in 20 mM Tris–HCl (pH 7.5) and 100 mM NaCl. For electrophoretic mobility shift assays, three DNA samples were used: 0.5 ng of single-stranded 60 bp, 20 ng of 58 bp, and 28 ng of 30 bp double stranded. DNA was incubated with different amounts of protein (0–25 µg) at room temperature for 30 min in 20 mM Tris (pH 7.5), 100 mM NaCl. The mixture was loaded on a pre-cast 10% non-denaturing polyacrylamide gel, and the gel was run at a constant voltage (120 V) with pre-chilled 0.5× TBE (89 mM Tris base, 89 mM boric acid, 1 mM EDTA (pH 8.0)) buffer at 4 °C. After the run was completed, the gel was stained with 1× SYBR™ green (Invitrogen) DNA stain solution for 30 min in the dark and imaged, and then stained with Coomassie blue to visualize the protein. The intrinsic fluorescence spectrum of the sRI–sT complex was recorded on a Cary Eclipse fluorescence spectrophotometer. One hundred microliters of the protein at 40 µg/ml in 20 mM Tris (pH 7.5), 100 mM NaCl was titrated with DNA ligands by adding 0.5–1 µl of ligand stock solution for each concentration point into the same cuvette and gently mixed by pipetting. Fluorescence spectra were recorded at 280-nm excitation wavelength. Fluorescence intensity was recorded at the peak wavelength of 320 nm for 8–12 concentration points for each tested ligand to determine apparent  $K_d$  values. The change in fluorescence did not vary over time, so the measurements were collected directly after mixing, without any additional incubation. No quenching was observed for a negative control protein (purified malate synthase from *Mycobacterium tuberculosis*) when mixed with these DNA ligands. The relative change in fluorescence intensity was plotted against final ligand concentration on a double reciprocal plot, with the slope recorded as a  $K_d$  value. Each titration was done twice, and the average of two  $K_d$  values is given in the Table 4; the resultant  $K_d$  values differed no more than by 5% between two replicates.

## Accession numbers

The structures presented in this work are deposited in the PDB database under the accession numbers PDB: 6PSH, 6PSK, 6PXE, 6PX4.

Supplementary data to this article can be found online at <https://doi.org/10.1016/j.jmb.2020.06.013>.

## Author Contributions

I.V.K. proposed the hypothesis, designed and performed experiments, analyzed the data, and wrote the manuscript. V.K., S.H.M., and J.-Y.C. performed experiments and analyzed the data. J.Z. supervised the EM structure determination. R.F.Y. and J.C.S. analyzed the data and wrote the manuscript.

## Acknowledgments

We would like to thank Ryan Hughes for the help with constructing expression vectors, the Advanced Photon Source (APS) beamlines 19ID and 23ID at Argonne National lab for the access for X-ray data collection, and Tracy Musa for reviewing and editing this manuscript. We thank the Microscopy and Imaging Center at Texas A&M University for providing instrumentation for data collection, and the Texas A&M High-Performance Research Computing Center for providing the computational resources for data processing. This work was supported by Welch Foundation grants A-0015 and A-1863, National Institutes of Health grant NIGMS 27099-40 and R35GM136396-01. We also acknowledge Texas A&M University's Center for Phage Technology and the Center for Structural Biology.

## Declaration of Competing Interests

The authors declare no competing interests.

Received 17 April 2020;

Received in revised form 10 June 2020;

Accepted 12 June 2020

Available online 17 June 2020

## Keywords:

lysis;  
holin;  
antiholin;  
SAR domain;  
domain swapping

†Current address: V. Kuznetsov, KBI Biopharma, 2 Triangle Dr., Research Triangle, NC 27709, USA.

‡Current address: S. Moussa, Entasis Therapeutics, Boston BioHub, 35 Gatehouse Drive, Waltham, MA 02451, USA.

## Abbreviations used:

LIN, lysis inhibition; SAR, signal anchor release; T, holin; RI, antiholin; VAST, vector alignment search tool.

## References

- [1] Kortright, Kaitlyn E., Chan, Benjamin K., Koff, Jonathan L., Therapy, Phage, (2019). A renewed approach to combat antibiotic-resistant bacteria *Cell Host Microbe*, **25**, (2) 219–232, <https://doi.org/10.1016/j.chom.2019.01.014>.
- [2] Jesse Cahill, R.Y., (2019). Phage lysis: multiple genes for multiple barriers. *Adv. Virus Res.*, **103**, 33–70 <https://doi.org/bs.aivir.2018.09.003>.
- [3] Ramanculov, E., Young, R., (2001). Genetic analysis of the T4 holin: timing and topology. *Gene.*, **265**, 25–36.
- [4] Young, R., (2002). Bacteriophage holins: deadly diversity. *J. Mol. Microbiol. Biotechnol.*, **4**, 21–36.
- [5] Tran, T.A.T., Struck, D.K., Young, R., (2005). Periplasmic domains define holin–antiholin interactions in t4 lysis inhibition. *J. Bacteriol.*, **187**, 6631–6640, <https://doi.org/10.1128/JB.187.19.6631-6640.2005>.
- [6] Moussa, S.H., Kuznetsov, V., Tran, T.A.T., Sacchettini, J.C., Young, R., (2012). Protein determinants of phage T4 lysis inhibition. *Protein Sci. Publ. Protein Soc.*, **21**, 571–582, <https://doi.org/10.1002/pro.2042>.
- [7] Ramanculov, E., Young, R., (2001). An ancient player unmasked: T4 *rl* encodes a t-specific antiholin. *Mol. Microbiol.*, **41**, 575–583.
- [8] Chen, Y., Young, R., (2016). The last *r* locus unveiled: T4 *RlII* is a cytoplasmic antiholin. *J. Bacteriol.*, **198**, 2448–2457, <https://doi.org/10.1128/JB.00294-16>.
- [9] Tran, T.A.T., Struck, D.K., Young, R., (2007). The T4 *Rl* antiholin has an N-terminal signal anchor release domain that targets it for degradation by DegP. *J. Bacteriol.*, **189**, 7618–7625, <https://doi.org/10.1128/JB.00854-07>.
- [10] Sun, Q., Kutty, G.F., Arockiasamy, A., Xu, M., Young, R., Sacchettini, J.C., (2009). Regulation of a muralytic enzyme by dynamic membrane topology. *Nat. Struct. Mol. Biol.*, **16**, 1192–1194, <https://doi.org/10.1038/nsmb.1681>.
- [11] Doermann, A.H., (1948). Lysis and lysis inhibition with *Escherichia coli* bacteriophage. *J. Bacteriol.*, **55**, 257–276.
- [12] Rutberg, B., Rutberg, L., (1965). Role of superinfecting phage in lysis inhibition with phage T4 in *Escherichia coli*. *J. Bacteriol.*, **90**, 891–894.
- [13] Anderson, C.W., Eigner, J., (1971). Breakdown and exclusion of superinfecting T-even bacteriophage in *Escherichia coli*. *J. Virol.*, **8**, (6) 869–886.
- [14] Gibrat, J.F., Madej, T., Bryant, S.H., (1996). Surprising similarities in structure comparison. *Curr. Opin. Struct. Biol.*, **6**, 377–385, [https://doi.org/10.1016/s0959-440x\(96\)80058-3](https://doi.org/10.1016/s0959-440x(96)80058-3).
- [15] Krissinel, E., Henrick, K., (2007). Inference of macromolecular assemblies from crystalline state. *J. Mol. Biol.*, **372**, 774–797, <https://doi.org/10.1016/j.jmb.2007.05.022>.
- [16] Bennett, M.J., Choe, S., Eisenberg, D., (1994). Domain swapping: entangling alliances between proteins. *Proc. Natl. Acad. Sci. U. S. A.*, **91**, 3127–3131, <https://doi.org/10.1073/pnas.91.8.3127>.
- [17] Holm, L., Rosenström, P., (2010). Dali server: conservation mapping in 3D. *Nucleic Acids Res.*, **38**, W545–W549, <https://doi.org/10.1093/nar/gkq366>.
- [18] Black, L.W., Ahmad-Zadeh, C., (1971). Internal proteins of bacteriophage T4D: their characterization and relation to head structure and assembly. *J. Mol. Biol.*, **57**, (1) 71–92.
- [19] F.Repoila, F., F.Tétart, F., J.-Y.Bouet, J.-Y., H.M.Krisch, H. M., (1994). Genomic polymorphism in the T-even bacteriophages. *EMBO J.*, **13**, (17) 4181–4192.
- [20] S.T.Abedon, S.T., (2019). Look who's talking: T-even phage lysis inhibition, the granddaddy of virus–virus intercellular communication research. *Viruses*, **11**, <https://doi.org/10.3390/v11100951>.
- [21] Paddison, P., Abedon, S.T., Dressman, H.K., Gailbreath, K., Tracy, J., Mosser, E., Neitzel, J., Guttman, B., et al., (1998). The roles of the bacteriophage T4 *r* genes in lysis inhibition and fine-structure genetics: a new perspective. *Genetics.*, **148**, 1539–1550.
- [22] R.White, R., S.Chiba, S., T.Pang, T., J.S.Dewey, J.S., C.G. Savva, C.G., A.Holzenburg, A., K.Pogliano, K., R.Young, R., (2011). Holin triggering in real time. *Proc. Natl. Acad. Sci. U. S. A.*, **108**, 798–803, <https://doi.org/10.1073/pnas.1011921108>.
- [23] . Xu, M., Struck, D.K., Deaton, J., Wang, I.-N., Young, R., (2004). A signal-arrest-release sequence mediates export and control of the phage P1 endolysin. *Proc. Natl. Acad. Sci. U. S. A.*, **101**, 6415–6420, <https://doi.org/10.1073/pnas.0400957101>.
- [24] Dall, E., Hollerweger, J.C., Dahms, S.O., Cui, H., Häussermann, K., Brandstetter, H., (2018). Structural and functional analysis of cystatin E reveals enzymologically relevant dimer and amyloid fibril states. *J. Biol. Chem.*, **293**, 13151–13165, <https://doi.org/10.1074/jbc.RA118.002154>.
- [25] Rousseau, F., Schymkowitz, J., Itzhaki, L.S., (2012). Implications of 3D domain swapping for protein folding, misfolding and function. *Adv. Exp. Med. Biol.*, **747**, 137–152, [https://doi.org/10.1007/978-1-4614-3229-6\\_9](https://doi.org/10.1007/978-1-4614-3229-6_9).
- [26] Huang, Q., Korte, T., Rachakonda, P.S., Knapp, E.-W., Herrmann, A., (2009). Energetics of the loop-to-helix transition leading to the coiled-coil structure of influenza virus hemagglutinin HA2 subunits. *Proteins.*, **74**, 291–303, <https://doi.org/10.1002/prot.22157>.
- [27] K.H. To, Young, R., (2014). Probing the structure of the S105 hole. *J. Bacteriol.*, **196**, 3683–3689, <https://doi.org/10.1128/JB.01673-14>.
- [28] Young, R., (2014). Phage lysis: three steps, three choices, one outcome. *J. Microbiol. Seoul Korea.*, **52**, 243–258, <https://doi.org/10.1007/s12275-014-4087-z>.
- [29] Moussa, S.H., Lawler, J.L., Young, R., (2014). Genetic dissection of T4 lysis. *J. Bacteriol.*, **196**, 2201–2209.
- [30] D.M.Masuwo Obinata, D.M., (1968). Intracellular localization of deoxyribonucleases in *Escherichia coli*. *Biochim. Biophys. Acta*, **155**, (1) 98–106.
- [31] W.Bode, W., (1967). Lysis inhibition in *Escherichia coli* infected with bacteriophage T4. *J. Virol.*, **1**, 948–955.
- [32] A.D.Hershey, A.D., (1946). Mutation of bacteriophage with respect to type of plaque. *Genetics.*, **31**, (6) 620–640.
- [33] Z.Otwinowski, Z., W.Minor, W., (1997). Processing of X-ray diffraction data collected in oscillation mode. *Methods Enzymol.*, **276**, 307–326.
- [34] G.M.Sheldrick, G.M., (2010). Experimental phasing with SHELXC/D/E: combining chain tracing with density modification. *Acta Crystallogr. D Biol. Crystallogr.*, **66**, 479–485, <https://doi.org/10.1107/S0907444909038360>.
- [35] Bricogne, G., Vonrhein, C., Flensburg, C., Schiltz, M., Paciorek, W., (2003). Generation, representation and flow of phase information in structure determination: recent developments in and around SHARP 2.0. *Acta Crystallogr. D Biol. Crystallogr.*, **59**, 2023–2030, <https://doi.org/10.1107/s0907444903017694>.
- [36] Adams, P.D., Afonine, P.V., Bunkóczi, G., Chen, V.B., Davis, I. W., Echols, N., Headd, J.J., Hung, L.-W., et al., (2010). PHENIX: a comprehensive python-based system for macromolecular structure solution. *Acta Crystallogr. D Biol. Crystallogr.*, **66**, 213–221, <https://doi.org/10.1107/S0907444909052925>.

- [37] Emsley, P., Lohkamp, B., Scott, W.G., Cowtan, K., (2010). Features and development of Coot. *Acta Crystallogr. D Biol. Crystallogr.*, **66**, 486–501, <https://doi.org/10.1107/S0907444910007493>.
- [38] Bruker AXS, (2018). PROTEUM3, Version 2018.1 Bruker AXS Inc., Madison, Wisconsin, USA, 2018.
- [39] W.K.S. Winn MD Ballard CC, Cowtan KD, Dodson EJ, Emsley P, Evans PR, Keegan RM, Krissinel EB, Leslie AG, McCoy A, McNicholas SJ, Murshudov GN, Pannu NS, Potterton EA, Powell HR, Read RJ, Vagin A., Overview of the CCP4 suite and current developments, *Acta Crystallogr. Biol. Crystallogr.* Apr 1;67(Pt 4) (2011) 235–42. <https://doi.org/10.1107/S0907444910045749>.
- [40] A.Vagin, A., A.Teplyakov, A., (1997). It MOLREP: an automated program for molecular replacement. *J. Appl. Crystallogr.*, **30**, 1022–1025, <https://doi.org/10.1107/S0021889897006766>.
- [41] Timothy Grant, N.G., (2015). Measuring the optimal exposure for single particle cryo-EM using a 2.6 Å reconstruction of rotavirus VP6. *ELife*, **4**.
- [42] K.Zhang, K., (2016). Gctf: real-time CTF determination and correction. *J. Struct. Biol.*, **193**, (1) 1–12.
- [43] G.Tang, G., L.Peng, L., P.R.Baldwin, P.R., D.S.Mann, D.S., W.Jiang, W., I.Rees, I., S.J.Ludtke, S.J., (2007). EMAN2: an extensible image processing suite for electron microscopy. *J. Struct. Biol.*, **157**, (1) 38–46.
- [44] S.H.S. Xiao-chen Bai EesonRajendra, S.H.S. Xiao-chen Bai Eeson, GuanghuiYang, Guanghui, YigongShi, Yigong, (2015). Sampling the conformational space of the catalytic subunit of human  $\gamma$ -secretase. *ELife*, **4**.
- [45] K.S. Leonardo G.Trabuco Elizabeth Villa, K.S. Leonardo G., KakoliMitra, Kakoli, JoachimFrank, Joachim, (2008). Flexible fitting of atomic structures into electron microscopy maps using molecular dynamics. *Structure*, **16**, 673–683.